Available online at www.sciencedirect.com
SCIENCE DIRECT®
Acta Materialia 52 (2004) 4447–4460
Acta MATERIALIA
www.actamat-journals.com

Nucleation mechanism of the eutectic phases in aluminum–silicon hypoeutectic alloys

Sumanth Shankar, Yancy W. Riddle, Makhlouf M. Makhlouf *

Department of Mechanical Engineering, Advanced Casting Research Center, Worcester Polytechnic Institute, Metal Processing Institute (MPI), 100, Institute Rd., Worcester, MA 01609, USA

Received 9 December 2003; received in revised form 10 May 2004; accepted 27 May 2004
Available online 17 July 2004

Abstract

A theory is presented to explain the mechanism of formation of the eutectic phases in Al–Si hypoeutectic alloys. Results include optical, scanning and transmission electron microscopy, as well as selected area electron diffraction analysis and elemental X-ray mapping performed on Al–Si hypoeutectic alloy samples. The alloy samples had precisely controlled chemistry and were solidified at various cooling rates. The data presented support the proposed theory with microstructural and crystallographic evidence.

Keywords: Al–Si; Eutectic; Nucleation; Mechanism; Hypoeutectic

1. Introduction

Al–Si alloys are some of the most widely used materials for casting domestic, military, automotive, and aerospace components [1]. Evolution of the eutectic structure during cooling of these alloys influences fluid flow during their final stages of solidification and hence controls the efficiency of liquid metal feeding into die cavities [2]. Feeding efficiency in turn affects shrinkage, which may cause porosity, and chemical segregation in cast parts making the mechanism of eutectic formation of particular scientific and industrial interest [2]. Moreover, upon addition of trace quantities of certain elements, such as Na or Sr, to a hypoeutectic Al–Si alloy, the structure of the eutectic Si phase transforms from a plate-like (*flake*) structure to a fine fibrous (*coral-like*) structure [3]. This morphological transformation significantly enhances the mechanical properties and overall performance of components that are cast from these alloys [4]. Consequently, much of the fundamental research in the Al–Si alloy system during the past 80 years has been directed towards understanding the mechanism behind the modification of the eutectic Si phase morphology by such trace element additions [3]. However, and despite many hypotheses proposed to explain the modification of the eutectic structure in hypoeutectic Al–Si alloys [3], the genesis of this technologically important morphological transformation remains uncertain. This is mainly due to the lack of conclusive evidence provided by experimentation in support of the proposed hypotheses. The main assumption underlying many popular hypotheses on the mechanism of modification of the silicon phase morphology is that the eutectic silicon phase nucleates on the primary aluminum dendrites during solidification of the hypoeutectic alloys and that the modifying trace elements inhibit the growth of the eutectic silicon phase, thus transforming the morphology of the Si phase from plate-like to fibrous [3,5–7]. Careful examination of these hypotheses shows that they cannot explain many observed phenomena that are associated with chemical modification, particularly: (1) they do not explain the relatively large undercooling during solidification that is observed with the evolution of the eutectic phases when modifying elements are present; (2) they cannot explain the occurrence of eutectic modification, and even

* Corresponding author. Tel.: +1-508-831-5647; fax: +1-508-831-5993.
E-mail address: mmm@wpi.edu (M.M. Makhlouf).

1359-6454/$30.00
doi:10.1016/j.actamat.2004.05.045

over-modification, without chemical additives, but rather due to an increased superheat and/or a relatively fast solidification rate [8,9]. These observations have led some researchers to suggest that modification of the eutectic Si morphology is caused by a large increase in Si nucleation events [10–14]. The present work does not seek to answer the unanswered questions related to modification of the Al–Si eutectic morphology, but rather it takes a step back to examine more critically the eutectic reaction in unmodified alloys. It is believed that a more complete understanding of the Al–Si eutectic reaction in the absence of chemical modifiers will shed light on the complicated mechanisms operating in chemically modified Al–Si alloys. Further research will build upon this base understanding by making modifying elements a separate degree of freedom, thus allowing critical reassessment of the relevant mechanisms that are active during modification to be further studied.

1.1. The aluminum–silicon system

The most recent review of the Al–Si binary system was by Murray and McAllister [15]. The system is a simple binary eutectic with limited solubility of aluminum in silicon and limited solubility of silicon in aluminum. The solubility of silicon in aluminum reaches a maximum 1.5 at.% at the eutectic temperature, and the solubility of silicon decreases to 0.05 at.% at 300 °C. The only invariant reaction in the system, other than the melting of pure Al and pure Si, is a eutectic transformation of liquid solution to solid solution Al and nearly pure Si, namely:

$$L \rightarrow Al_{eut} + Si_{eut}.$$

It is now widely accepted that this eutectic reaction occurs at 577.6 °C and 12.6% silicon. [1] However, it has recently been shown by Cantor and coworkers [11–14] that binary Al–Si alloys prepared from pure materials (99.999% purity Al and 99.9999% purity Si) can have up to 50 ppm iron. Although this level of iron is normally considered a trace level impurity of little consequence, the current work establishes its significant role in the formation of the Al–Si eutectic. It will be shown that iron, except when present in exceedingly low amounts ($\leqslant 0.0015\%$), results in the formation of iron containing β-(Al, Si, Fe) phase that plays an important role in the nucleation of the eutectic phases. Therefore, it is more appropriate to think of this system when discussing the eutectic reaction as essentially an Al–Si–Fe ternary system with the eutectic phases being $Al_{eut} + Si_{eut}$ + β-(Al, Si, Fe), rather than a binary Al–Si system. Table 1 shows typical levels of iron in various "*high-purity*" Al–Si alloys.

[1] Unless otherwise stated, all compositions are in wt%.

Table 1
Typical levels of iron in "*high-purity*" Al–Si alloys [14]

Purity of Al–Si alloy (%)	Fe (%)
99.99	0.0050
99.999	0.0025–0.0030
99.9999	$\leqslant$0.0015

2. Materials and procedures

2.1. Alloy chemistry and casting conditions

The two hypoeutectic Al–Si alloys used in this work and the materials from which they were constituted are shown in Table 2. The alloy chemistries were measured using spark transmission spectrometry [2,3] and results confirmed by measuring with Inductively Coupled Plasma (ICP) Atomic Emission Spectroscopy.

Each batch of alloy A was melted in a new high purity alumina crucible and thermally equilibrated at 750 °C for 1 h before being allowed to solidify. Since the nucleation and growth kinetics of the eutectic phases may be cooling rate dependent, specimens of the alloy were solidified using different cooling conditions that resulted in a wide range of cooling rates. These cooling conditions included furnace cooling (FC), air cooling (AC), and directional solidification (DS) [4] on a copper block held at room temperature. In each case, the cooling rate was measured from temperature vs. time data obtained during solidification and was considered to be the cooling rate in the liquid just before the first solid has formed. The effective cooling rates of alloy A samples are summarized in Table 3 and encompass cooling rates typical of industrial casting processes with the probable exception of high-pressure die casting. In addition, and in order to follow the progress of the eutectic reaction during solidification, additional alloy A samples were quenched after about 20 vol% of the eutectic had formed in a mixture of antifreeze and dry ice equilibrated at −40 °C.

Each batch of alloy B was melted in a new high purity graphite crucible and thermally equilibrated at 750 °C for 1 h before being allowed to solidify. Alloy B samples were cooled only in air at a cooling rate of 48 °C/min.

[2] Model Spectro Lab-Max LMXM3, Spectro Analytical Instruments, Fitchburg, MA, USA.

[3] Accuracy of the spark transmission spectrometer is Si ± 0.3, Fe ± 0.0003 when Fe < 0.01, and ±0.0022 when Fe > 0.1. Other relevant elements show negligible measurement errors.

[4] The DS samples were cast in a 7.5-cm long high purity alumina cylinder placed on a chilled copper block. The wall thickness of the cylinder was 2.5 cm and the cylinder was insulated with a 5-cm thick thermal insulating material.

Table 2
Chemistry of Al–Si alloys and the materials used to prepare them

Alloy	Raw materials		Chemical analysis						
	Al	Si	Si	Fe	P	Cu	Mn	Mg	Al
A	99.95	99.9999	7.45	0.0637	0.000857	0.003194	0.003100	0.000340	Bal.
B	99.999	99.9999	4.5–12.5	0.003309–0.004899	0.000342–0.000588	0.002430–0.006533	<0.0005	<0.00001	Bal.
Raw A	99.95	–	0.0661	0.004814	0.000529	0.005640	0.001000	0.002078	99.906
Raw B	99.999	–	<0.0006	0.002679	0.000524	0.001461	<0.0005	<0.00001	99.994

Table 3
Cooling rates for alloy A variants

Solidification condition	Cooling rate (°C/min)
Furnace cooling	1
Air cooling	48
Directional solidification	200

2.2. Thermal analysis

The two-thermocouple technique devised by Bäkerud et al. [16] was used for all thermal analyses. In this method, two thermocouples are located in the crucible such that one is near the crucible edge and the other is at its center. The time-based derivatives (dT/dt) from the data of these two thermocouples are obtained and plotted together with the difference in their temperature (ΔT) readings at a given time. The melt mass was approximately 100 g and the solidification rate from the 750 °C initial melt temperature was 48 °C/min.

2.3. Sample preparation, microscopy, and energy dispersive spectroscopy

Optical microscopy. A Nikon Epiphot metallograph was used for all optical microscopy. Samples for optical microscopy were mechanically ground to 4000 grit finish then electropolished for 5 s at 45 V using a mixture of 100 mL perchloric acid, 100 mL diethyl-monobutyl-ether, and 600 mL ethanol.

Scanning electron microscopy. The scanning electron microscopy (SEM) used was a JSM 840 equipped with a LaB_6 electron source operating at 15 keV and a Kevex energy dispersive spectrometer (EDS) system. Samples for SEM were prepared in the same manner as those prepared for optical microscopy.

Transmission electron microscopy. A 100 keV LaB_6 JEOL 100C TEM and a 200-keV CFEG Hitachi HF2000 TEM were used to investigate crystallographic relationships between the various eutectic phases and for chemical microanalysis. The HF2000 TEM was equipped with a Noran^{TM} EDS detector. Foils for transmission electron microscopy were prepared from specific locations in each sample by focused ion beam (FIB) milling [17] using an FEI 235 dual-focused gallium ion beam mill. Fig. 1 shows typical SEM micrographs of the samples and typical locations in the microstructure where transmission electron microscopy (TEM) foils were prepared. Several similar TEM samples were prepared and analyzed from each alloy varaint and cooling condition in order to ensure that the results were not anomolous.

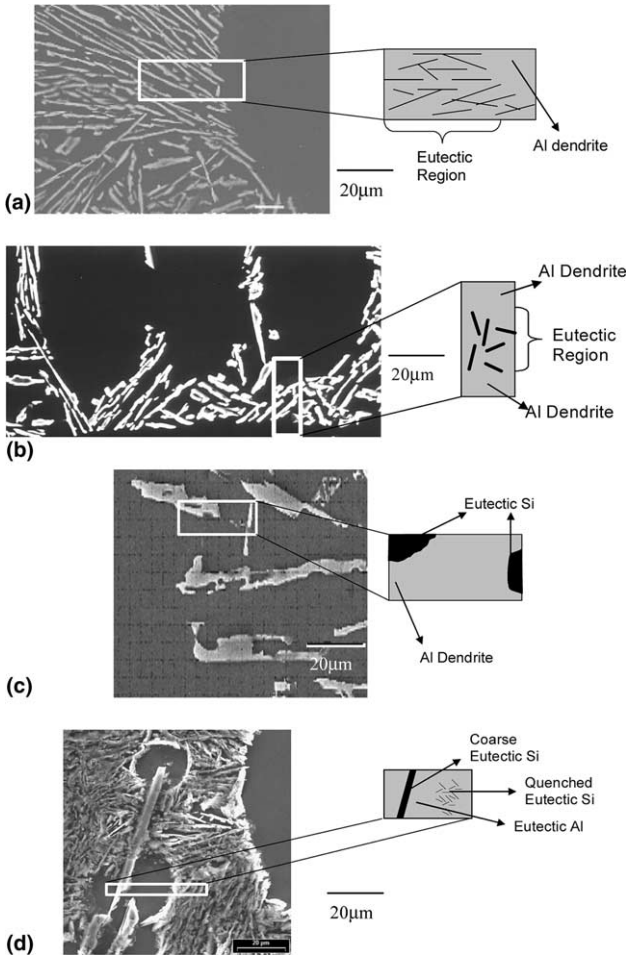

Fig. 1. SEM micrographs of samples used to prepare TEM foils. The white box drawn in the microstructures shows the location where the TEM sample was milled out by FIB. The schematic adjoining each micrograph illustrates the microstructure observed in the TEM sample after FIB milling: (a) Al–7wt%Si – directionally solidified casting (A-DS); (b) Al–7wt%Si – air cooled casting (A-AC); (c) Al–7wt%Si – furnace cooled casting (A-FC); (d) Al–7wt%Si – quenched after 20% of the eutectic reaction was completed (A-IQ).

Energy dispersive spectroscopy. A Noran detector run by ESVision v4.0 software was used to perform the energy dispersive spectroscopy. Dead time was limited to about 12% to ensure good peak-to-background ratio with a collection time of 200 s to provide significant counts/peak for quantitative analysis after ZAF correction. All TEM EDS work was performed on the Hitachi HF2000 microscope, which has a resolution for chemical microanalysis better than 20 nm.

Crystallography. Orienting the aluminum and silicon crystals to low index planes allowed crystallographic characterization. The various zone axes onto which each of the aluminum and silicon phases was oriented were B = ⟨100⟩, ⟨110⟩, ⟨111⟩, ⟨012⟩, ⟨113⟩, ⟨122⟩, ⟨013⟩,

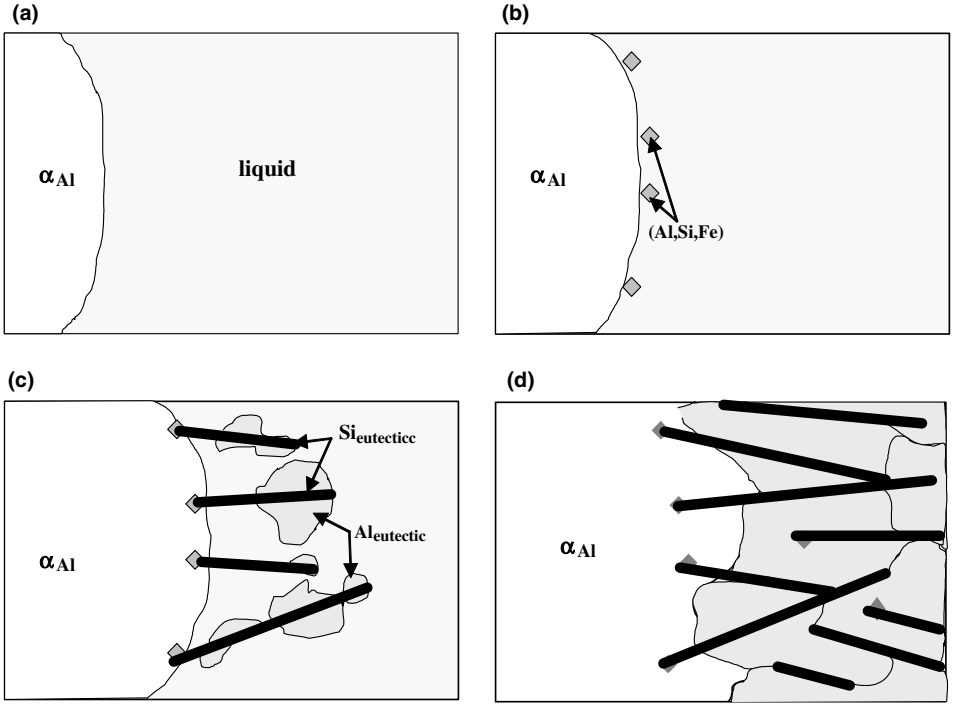

Fig. 2. Sequence of events during nucleation of eutectic phases in Al–Si hypoeutectic alloys: (a) growth of Al dendrites, (b) Nucleation of β-(Al, Si, Fe) phase, (c) nucleation of eutectic Si on the β-(Al, Si, Fe) phase in the solute field ahead of the primary aluminum, nucleation of eutectic Al on eutectic Si, and growth of eutectic Al; (d) impingement of dendrites and eutectic Al grains resulting in arrest of the growth of dendrites and further nucleation and growth of the eutectic phases.

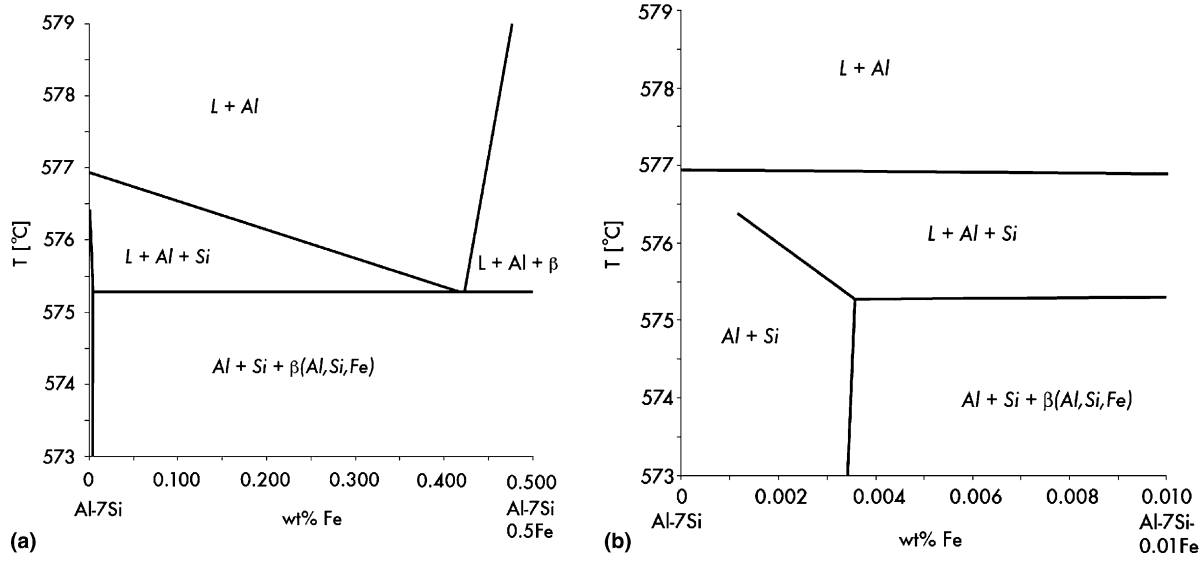

Fig. 3. Isopleths from the Al–Si–Fe ternary phase diagram obtained from the commercial software Pandat®.

⟨112⟩ and ⟨023⟩. In most cases, if there was a crystallographic relation between two phases, it was seen with one of these planes on the zone axis. Two crystals were said to have a crystallographic relationship between them when one crystal, oriented on a zone axis, also revealed a nearly centered zone axis in the second crystal. The absence of a strong zone axis alignment between two crystals was used to describe neighboring crystals as having no crystallographic relationship. When a crystallographic relation was found between an aluminum phase and a silicon phase, selected area diffraction (SAD) patterns were obtained. The diffracting conditions were calibrated and input in the program specifically for the Hitachi HF2000 TEM used in this work. A minimum of three SAD patterns; one from the silicon phase, one from the aluminum phase, and one including both the silicon and aluminum phases, were obtained in order to compare the diffraction patterns and confirm the crystallographic relationship. In addition, bright field and dark field images were obtained in order to confirm that the phases had a specific crystallographic orientation relationship.

Classical heterogeneous nucleation theory states that when an interface between a solid and a liquid is in part replaced by a lower energy solid–solid interface successful nucleation of the new solid is energetically favored when it does not significantly alter the geometrically critical radius value [18]. Since an interface of two solid phases where both phases exhibit some specific crystallographic orientation between them has less energy than that interface in a random configuration, the oriented interface is more likely to form than the un-oriented interface. However, it should be pointed out that this investigation is concerned with the nucleation and growth of phases occurring during liquid-to-solid transformation. As such, it is recognized that

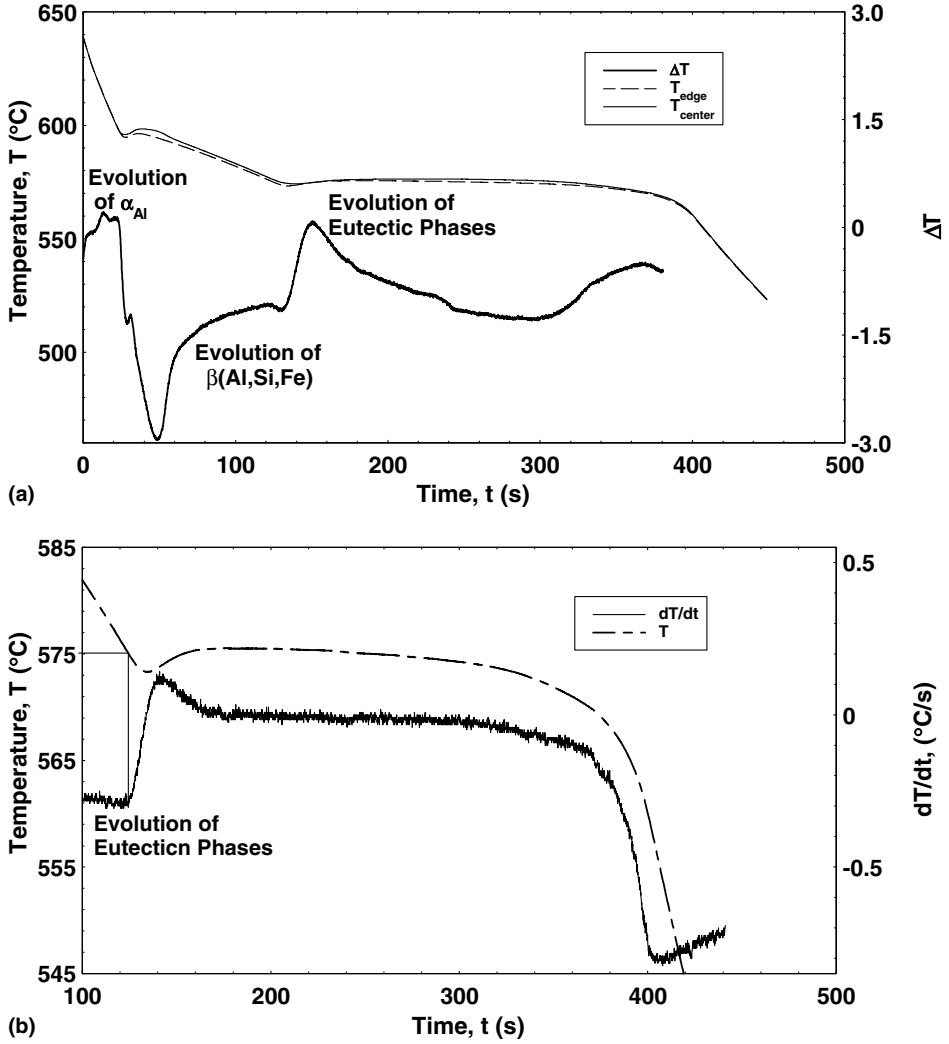

Fig. 4. Solidification curve obtained using the two-thermocouple technique [18] for Al–8.5%Si–0.0032%Fe alloy. Figure (a) shows the sequence of phase evolution during soldification. Figure (b) is a "*zoom in*" on (a) with $\partial T/\partial t$ also plotted in order to clearly show the nucleation temperature of the eutectic phases in this alloy.

several preferred crystallographic orientations between emerging phases must have existed at their times of inception, and would satisfy a lowest-energy configuration for nucleation. Therefore, in support of the proposed theory, it is sufficient to show evidence of a preferred relationship between adjoining phases, which in this case can be best described as having parallel directions. This does not uniquely establish a full crystallographic relationship between two crystals, which is often the case for solid-to-solid transformations, as we do not supply unique crystallographic directions and planes. The quantity of crystals satisfying a parallel direction criterion with neighboring crystal(s) is evidence of a preferred lowest energy nucleation environment having occurred locally during solidification and is referred to here, even though not fully meeting the formal definition, as a "*crystallographic relationship*". It should also be pointed out that, although the presence of such a relationship between a nucleus and a solid forming from a melt may point to the possibility that the solid has nucleated on the specific nucleus, it is not a sufficient condition. Nevertheless, when combined with abundant visual evidence from scanning and transmission electron microscopy, and supported with thermodynamic and thermal analyses, orientation relationships can be a valuable tool in differentiating the sequence of precipitation events during a liquid-to-solid transformation such as a eutectic reaction.

3. Results and discussion

3.1. Proposed theory

Based on this work, it is proposed that nucleation of the eutectic phases in Al–Si hypoeutectic alloys proceeds as illustrated schematically in Figs. 2(a)–(d). During solidification, the primary aluminum phase forms as dendrites at the liquidus temperature of the alloy. This is followed by the evolution of a secondary β-(Al, Si, Fe) phase at some temperature between the liquidus temperature and the eutectic temperature of the alloy depending on the concentration of Fe in the alloy. At the eutectic temperature, and at an undercooling of 0.4C–0.8 °C, eutectic silicon (Si_{eut}) nucleates on the secondary β-(Al, Si, Fe) phase in the solute field ahead of the growing aluminum

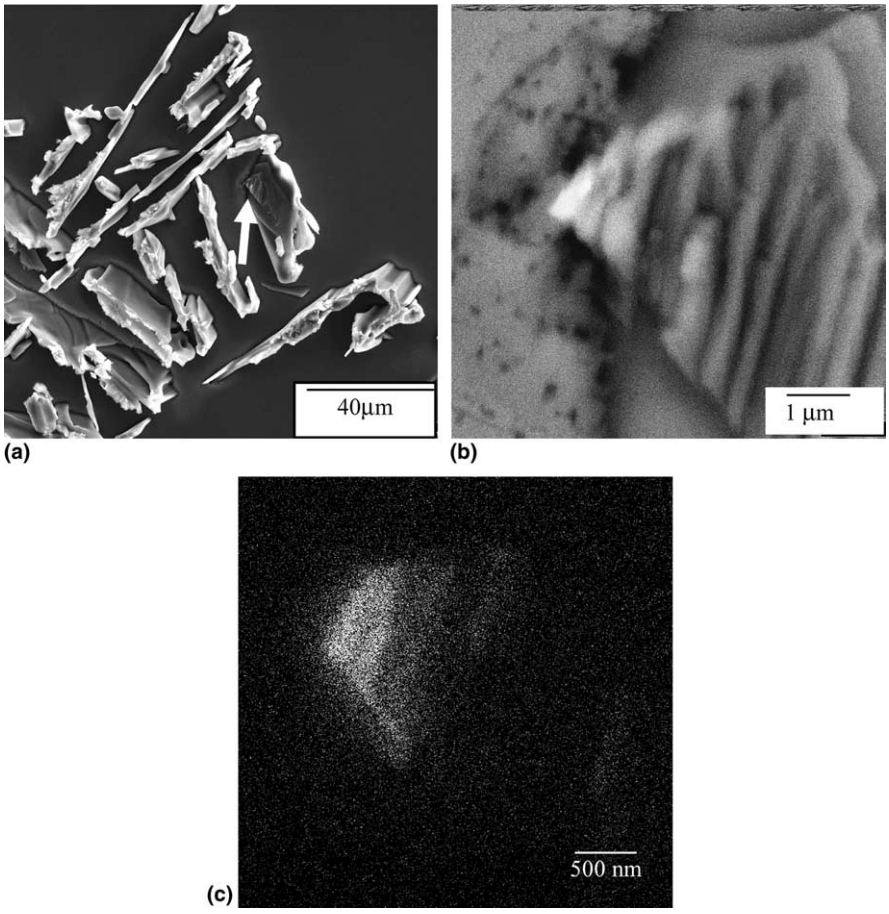

Fig. 5. SEM micrographs of B (Al–4.5%Si) alloy samples: (a) secondary electron image; (b) backscattered electron image of region indicated by arrow in (a); (c) elemental map of Fe showing the β-$Al_9Si_2Fe_2$ precipitate.

Table 4
Composition of (Al, Si, Fe) particles similar to that in Fig. 5

Element	Particle #1		Particle #2		Particle #3		Particle #4		Particle #5	
	wt%	at.%	wt%	at.%	wt%	at.%	wt%	at.%	wt%	at.%
Al	63.64	73.66	62.8	69.2	62.83	72.98	64.59	74.58	61.53	70.95
Si	10.86	12.08	12.43	15.42	11.10	12.39	10.26	11.38	13.82	15.31
Fe	25.49	14.26	24.77	15.38z	26.07	14.63	25.15	14.03	24.65	13.73

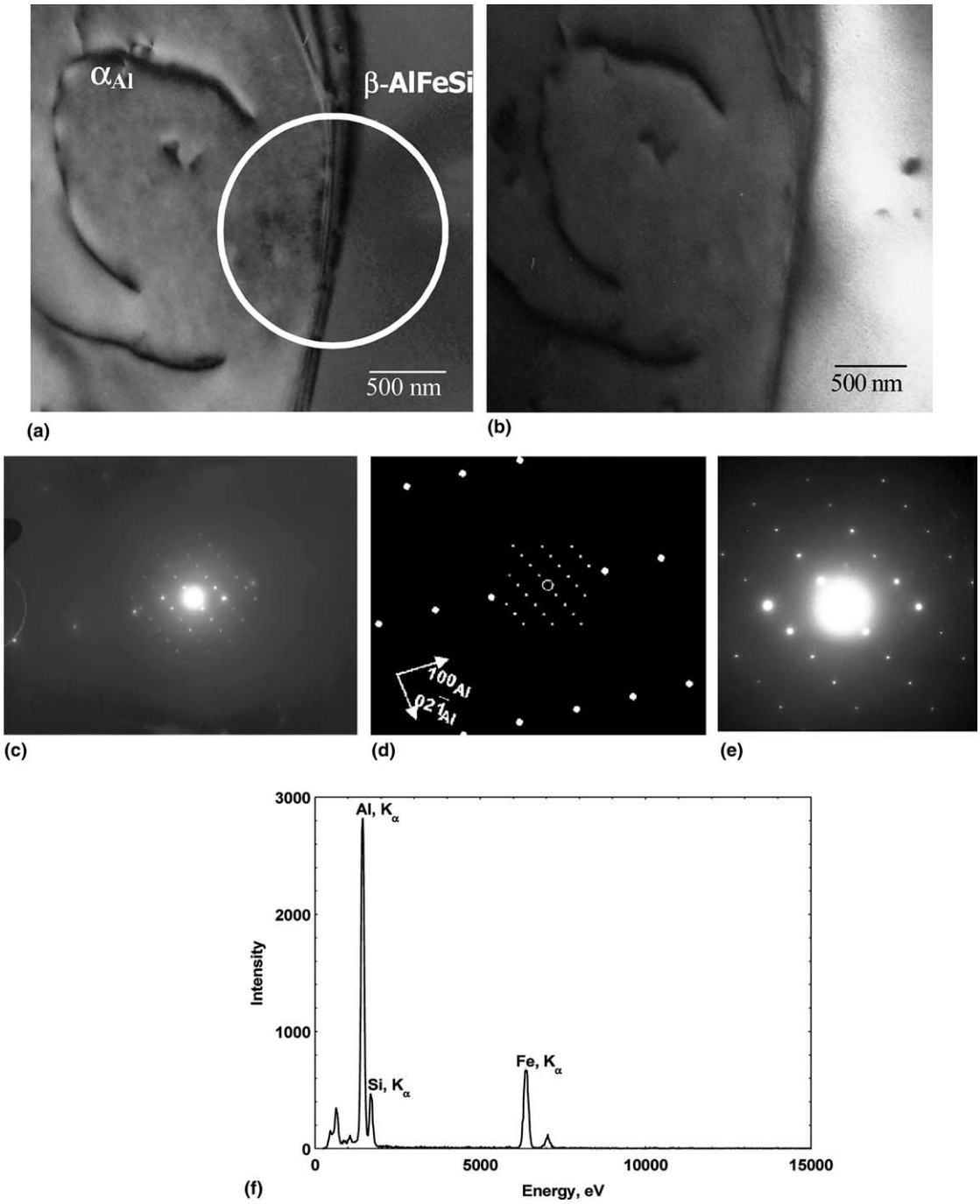

Fig. 6. Interface between α-aluminum dendrite (α_{Al}) and β-$Al_9Si_2Fe_2$: (a) bright field TEM image; (b) centered dark field image showing the β-$Al_9Si_2Fe_2$ phase; (c) SAD pattern taken in the encircled region in (a), (d) digital replication of (c) for better visualization; (e) SAD pattern from the β-$Al_9Si_2Fe_2$ phase brought to a zone axis; (f) EDS spectrum obtained from the β-$Al_9Si_2Fe_2$ particle.

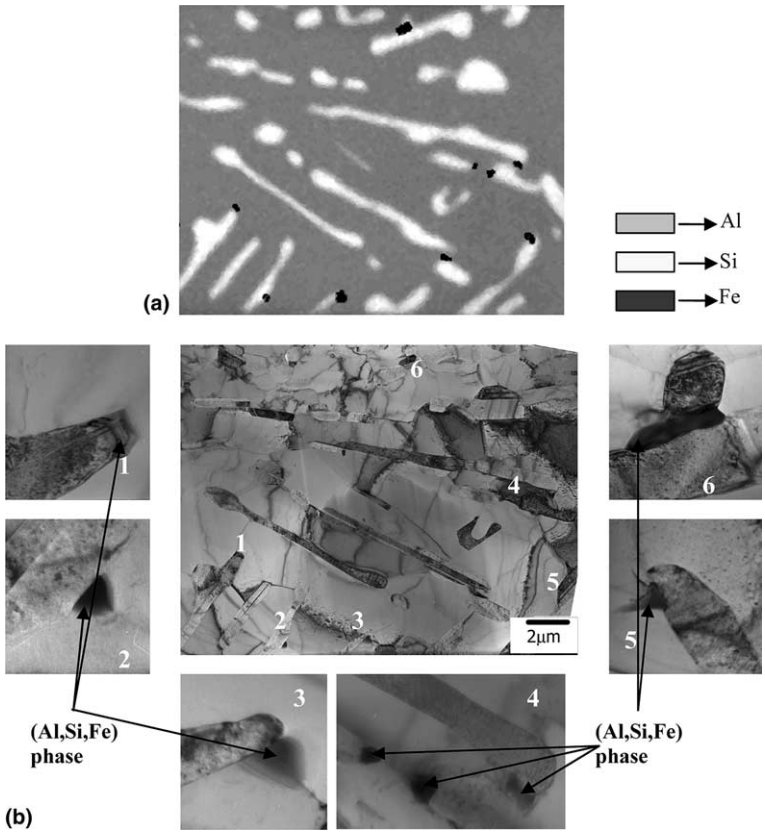

Fig. 7. Images showing association of β-(Al, Si, Fe) phase with eutectic Si: (a) composite elemental map of Al, Si and Fe (key given) obtained from the image shown in (b); (b) TEM bright field image showing locations where β-(Al, Si, Fe) phases were found.

dendrites. Once nucleated, the eutectic silicon grows as flakes into the eutectic liquid. The liquid surrounding the eutectic silicon flakes become enriched with aluminum as it is being depleted of silicon; consequently, eutectic aluminum (Al_{eut}) nucleates and grows on the edges and tips of the eutectic silicon flakes. Finally, the aluminum dendrites stop growing upon impingement with the growing eutectic aluminum grains.

The following sections substantiate this mechanism of nucleation of the eutectic phases in hypoeutectic Al–Si alloys with thermodynamic and thermal analyses results, as well as results of optical, scanning and transmission electron microscopy, selected area electron diffraction analysis, and elemental X-ray mapping.

3.2. Formation of β-(Al, Si, Fe)

Fig. 3 shows isopleths from an Al–7Si equilibrium phase diagram with increasing Fe content as calculated using the commercial software Pandat® [5] version 4-O–H. Pandat® uses the PanAluminum® version 2b thermodynamic database for commercial aluminum alloys, which is experimentally verified with published limits of usability for the elements in this calculation, namely Al > 80%, Si < 17.45%, Fe < 1.0%. Comparable results were obtained from the commercial software Thermocalc® [6] using the Thermotech Aluminum database. At a minimum of 0.0038% Fe, a ternary β-(Al, Si, Fe) phase is expected to form at 575 °C. Since this level of Fe has been shown to be a natural impurity level in even "*high-purity*" Al (see Table 1), the system must be thought of as a ternary Al–Si–Fe system and not a binary Al–Si system. Moreover, the equilibrium partition coefficient of Fe in the system is about 0.022 [19,20] suggesting enrichment of the iron solute atoms ahead of the solid–liquid interface during solidification. Therefore, even these trace quantities of Fe in Al ensure the invariant reaction to be:

$$L \rightarrow \alpha_{Al} + \beta - (Al, Si, Fe) + Si_{eut}.$$

Rivlin [21] and Richards [22] have shown that in the compositional ranges of hypoeutectic Al–Si alloys, if the local iron concentration in the solute field ahead of the aluminum dendrites reaches 0.05%, precipitation of the β-($Al_9Si_2Fe_2$) phase will occur. Thus, β-(Al, Si, Fe) precipitates just before the eutectic silicon, or along with

[5] Pandat® is marketed by CompuTherm, LLC, Madison, WI, USA.

[6] Thermolcalc® is developed and marketed by the Foundation of Computational Thermodynamics, Stockholm, Sweden.

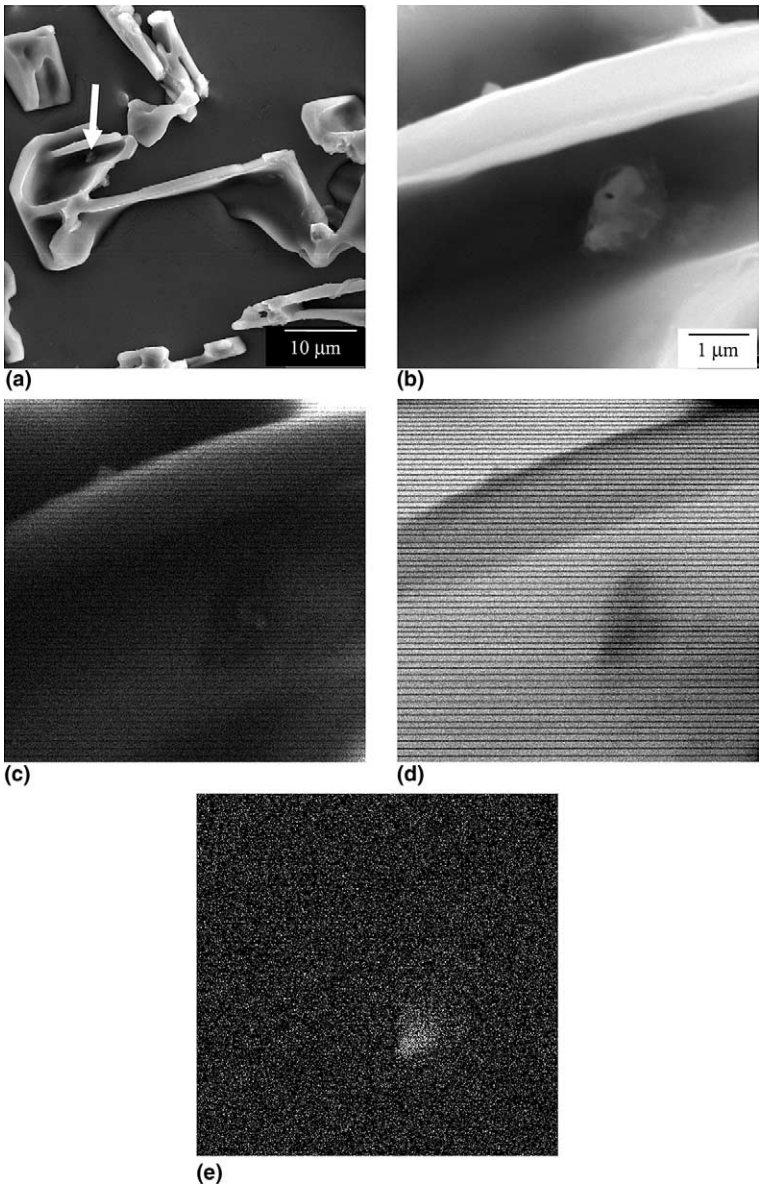

Fig. 8. Elemental map of B (7wt%Si) alloy showing β-(Al, Si, Fe) phase as a nucleant for eutectic Si: (a) low magnification secondary electron image of the microstructure; (b) high magnification secondary electron image of the location pointed in (a); (c), (d) and (e) are elemental maps obtained at the location pointed in (a) showing the distribution of Al, Si, and Fe, respectively.

the eutectic silicon depending on the iron content of the alloy, and in turn the β-(Al, Si, Fe) particles may nucleate the eutectic silicon.

Fig. 4(a) shows a typical thermal analysis curve for an Al–8.5%Si–0.0032%Fe alloy, showing the formation of the primary aluminum dendrites, followed by precipitation of the β-(Al, Si, Fe) phase, and then the eutectic phases. Although thermal analysis is useful for identifying the temperature at which phase precipitation events occur, it is insufficient for uniquely identifying the precipitating phases. However, as shown in the following paragraphs, these thermal analyses data correlate well with TEM observations and calculated phase diagrams giving confidence to the stated sequence of precipitation events. Calculations using the commercial software Pandat® suggest that this sequence of events occurs in hypoeutectic Al–Si alloys regardless of their Fe content for Fe contents up to 1.65%. Fig. 4(b) is a "zoom-in" on Fig. 4(a) and also shows the variation in dT/dt with time t. Note that the eutectic reaction, which according to the current Al–Si phase diagram [15] should occur at 577.6 °C, is delayed and occurs in this alloy at 575.1 °C. This delay may be attributed to the scarcity of the Si_{eut} nucleating β-(Al, Si, Fe) phase caused by the very low Fe content of this alloy. Fig. 4 reinforces the argument that the β-(Al, Si, Fe) phase plays a critical role in the nucleation of the eutectic Si phase.

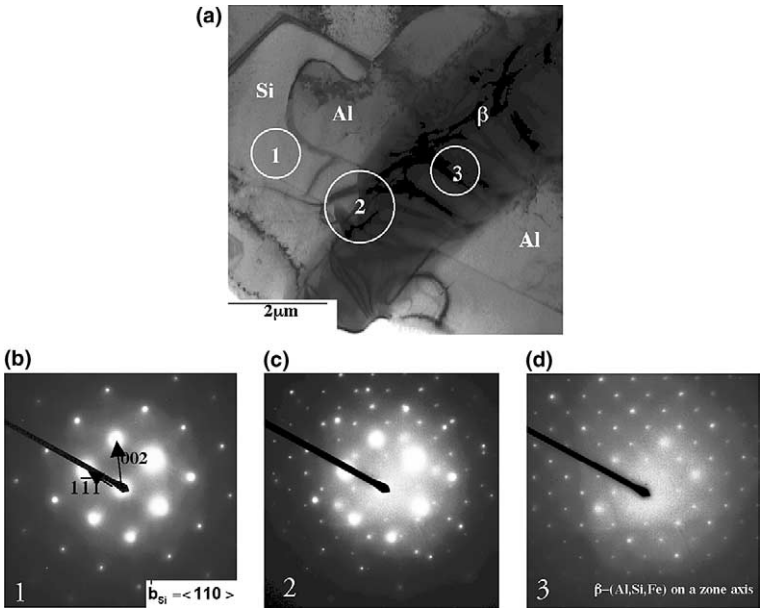

Fig. 9. Crystallographic relationship between β-(Al, Si, Fe) and Si. (a) Bright field TEM image. (b), (c), and (d) selected area diffraction patterns from the regions marked 1, 2 and 3 in (a). The region marked "1" is on Si, the region marked "2" is on the interface between β-(Al, Si, Fe) and Si, and the region marked "3" is on β-(Al, Si, Fe). The diffraction patterns show a distinct crystallographic relationship between β-(Al, Si, Fe) and Si. The sample used to generate this figure is Al–7Si–0.24Fe – air cooled at 48 °C/min.

Fig. 5 shows an (Al, Si, Fe) particle in a B alloy (4.5%Si) sample. Figs. 5(a) and (b) are SEM images of the particle taken in secondary electron mode and in backscatter electron mode, respectively. Fig. 5(c) is an elemental X-ray map of the same particle showing its Fe content. Table 4 shows the composition of a few (Al, Si, Fe) particles as obtained by EDS using a spot beam with a selected area diameter of 50 nm in the 200-kV TEM. It is evident that the average composition of these particles closely matches that of β-($Al_9Si_2Fe_2$), namely 69.2at.%Al, 15.4at.%Fe, and 15.4at.%Si [21].

3.3. Relationship between α-Al and β-(Al, Si, Fe)

The thermodynamic calculations and thermal analysis in Figs. 3 and 4 clearly indicate that the first solid to form is α-Al dendrites followed by β-(Al, Si, Fe) particles. Fig. 6 shows a preferred orientation relationship between α-Al dendrites and the β-(Al, Si, Fe) particles. Fig. 6(a) is a bright field TEM image of the interface between an α-Al dendrite and a β-(Al, Si, Fe) particle with the β-(Al, Si, Fe) particle oriented on a zone axis. Fig. 6(b) is a centered dark field image showing the β-(Al, Si, Fe) phase. Fig. 6(c) is a SAD pattern obtained from the encircled region in Fig. 6(a) and shows that there is a preferred crystallographic relationship between α-Al dendrites and the β-(Al, Si, Fe) particles. Fig. 6(d) is a digital replication of the diffraction pattern introduced for clarity. Fig. 6(e) shows an SAD pattern from the β-($Al_9Si_2Fe_2$) particle taken with a 200-kV TEM with a selected area diameter of 50 μm centered on the β-(Al, Si, Fe) particle and a camera length of 1.20 m. The SAD pattern in Fig. 6 shows that β-(Al, Si, Fe) is oriented on a zone axis. Fig. 6(f) is an EDS spectrum obtained from the β-(Al, Si, Fe) phase shown in Fig. 6(a). The composition of β-(Al, Si, Fe) calculated from the EDS spectrum in Fig. 6(f) is given as particle #4 in Table 4. The bright field image, centered dark field image, diffraction patterns, and EDS analyses strongly suggest that the β-(Al, Si, Fe) phase has nucleated on the α-Al dendrites.

3.4. Relationship between β-(Al, Si, Fe) and Si_{eut}

In 1963, Chadwick [10] hypothesized that eutectic silicon does not nucleate on α-Al dendrites, but rather on heterogeneous sites that are present in the solute field ahead of the dendrites. While Chadwick did not explicitly name β-(Al, Si, Fe) particles as those nucleants, Yang et al. [19] and Kalifa et al. [20] suggested that β-(Al, Si, Fe) could be a nucleant for eutectic Si in Al–Si alloys.

Fig. 7 is a composite of several TEM micrographs showing the association of eutectic Si with the β-(Al, Si, Fe) phase. Fig. 7(a) is a composite image obtained by combining the results of elemental maps for Al, Si and Fe, respectively, from the TEM bright field image shown in Fig. 7(b). Almost every eutectic silicon flake in the microstructure has a β-(Al, Si, Fe) particle attached to its edge. Moreover, several β-(Al, Si, Fe) particles are attached to more than one eutectic silicon flake that show differing crystallographic orientations

from one another. Similarly, Fig. 8 shows SEM micrographs, together with elemental X-ray maps, of an alloy B sample containing 7wt%Si. The presence of an iron rich phase attached to the eutectic Si is evident. Fig. 9 shows a representative TEM micrograph, selected area diffraction patterns, and crystallographic relationships between the β-(Al, Si, Fe) phase and eutectic silicon. It is evident from Fig. 9 that there is a distinct crystallographic relationship between the β-(Al, Si, Fe) phase and eutectic Si.

Finally, it should be mentioned that, while Mondolfo [23], and later Bercovici [24], showed that aluminum phosphide can be a powerful nucleating agent for silicon in *hypereutectic* Al–Si alloys, it has not been explicitly established that AlP is the only heterogeneous nucleant for eutectic Si in *hypoeutectic* Al–Si alloys. Moreover, no AlP particles were found in the SEM samples or TEM foils of this study.

3.5. Relationship between Si_{eut} and Al_{eut}

Figs 10–13 show representative TEM micrographs and crystallographic relationships between the various phases in typical microstructures from samples cast using the cooling rates described in Table 3. Fig. 10 demonstrates typical results obtained from A-DS samples. The TEM image shown is representative of this alloy and this solidification condition, and the adjoining illustrative schematic was drawn to scale from this micrograph. The interfaces and boundaries of the aluminum grains and the silicon phase in the schematic were carefully drawn after consulting many similar TEM micrographs at various magnifications and orientations. Careful examination of A-DS samples revealed that there is no preferred crystallographic relationship between aluminum dendrites and any of the eutectic aluminum or eutectic silicon phases. However, preferred

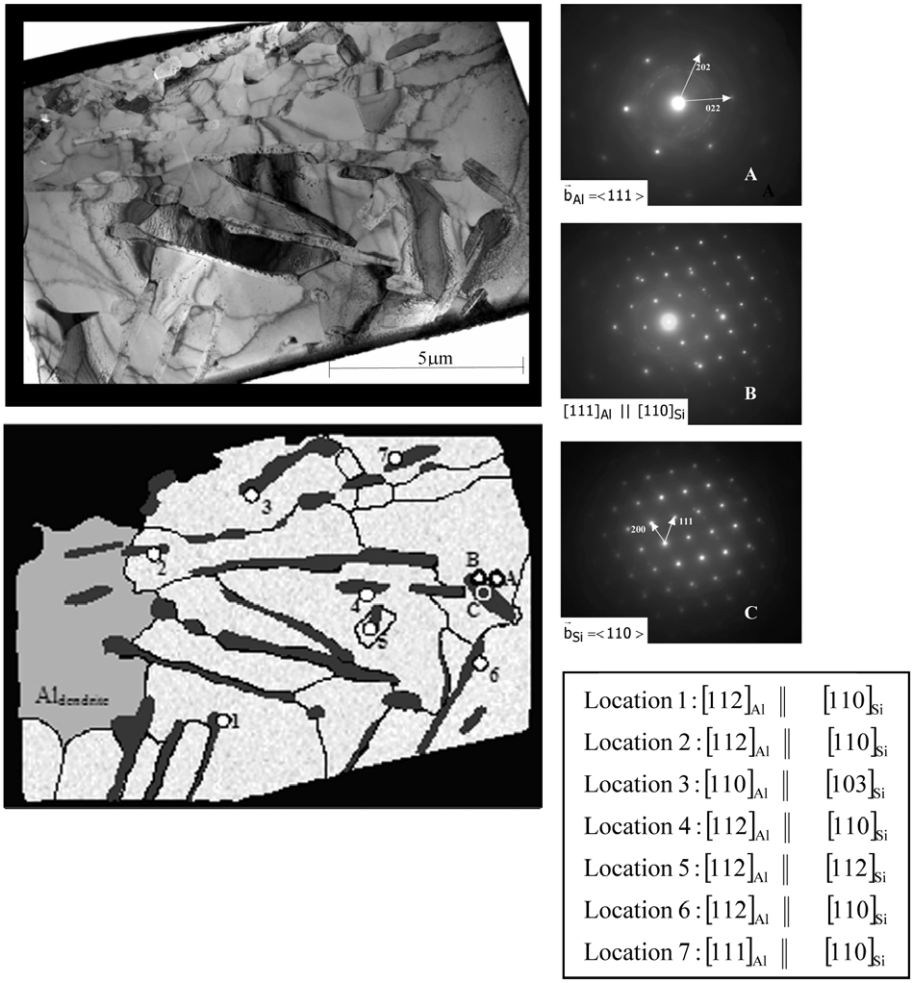

Fig. 10. Summary of TEM analysis of A-DS alloy. A schematic of the TEM image is shown to highlight the α-Al dendrite, eutectic Al grains, and eutectic Si flakes. The schematic is a 1:1 scale representation of the TEM micrograph. Crystallographic relations were observed between various eutectic Al grains and eutectic Si flakes and are shown in the image. One such crystallographic relationship is shown from a set of diffraction patterns obtained from eutectic Al, the interface between eutectic Al and Si, and eutectic Si; these are marked A, B, and C, respectively. The other crystallographic relationships observed between eutectic Al and eutectic Si were obtained from locations marked 1 through 7 in the schematic.

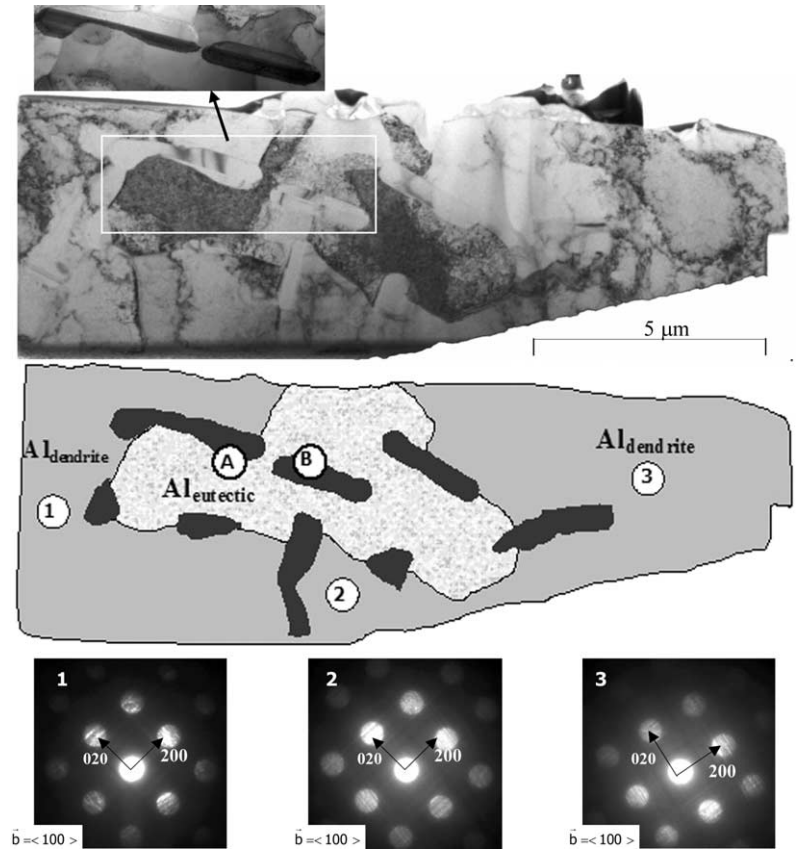

Fig. 11. Summary of TEM analysis of an A-AC casting. The TEM image was taken with the eutectic Al grain in the middle of the eutectic phases region oriented to the $[0\,1\,2]_{Al}$ zone axis. Also shown is schematic (drawn to scale) of the TEM image area to show the various phases in the microstructure. In addition, CBED patterns from the locations marked 1, 2 and 3, in the two α-Al dendrites and in the eutectic Al are shown. Analysis of Si twins revealed that the two Si flakes (shown in the top left enlarged TEM micrograph) are actually two parts of one large Si flake which has a discontinuity in the plane of the foil. SAD patterns from interfaces between eutectic Al and Si marked A and B revealed a crystallographic relationship: $[1\,1\,2]_{Al} \parallel [1\,1\,2]_{Si}$.

crystallographic relationships were always observed between eutectic silicon and eutectic aluminum. Many silicon flakes surround each eutectic aluminum crystal; however, only one such silicon flake was found to be partially encapsulated by a given eutectic aluminum crystal while the rest of the silicon flakes lie on the eutectic aluminum boundaries. Crystallographic relationships were always observed between the eutectic aluminum crystal and the particular eutectic silicon flake that was partially surrounded by it, while crystallographic relationships did not exist between the eutectic aluminum grain and any of the silicon flakes that lie on its boundaries. Each eutectic silicon flake was found to have one eutectic aluminum crystal with which it shared a crystallographic relationship. This same eutectic silicon and eutectic aluminum crystal pair always had the silicon flake partially encapsulated by the eutectic aluminum crystal.

Fig. 11 shows typical results obtained from A-AC samples. Similar to Fig. 10, the TEM image shown is representative of this alloy and this solidification condition. The adjoining illustrative schematic was drawn in a manner similar to the schematic in Fig. 10. In this micrograph, there are two dendrite arms, one on each side of the eutectic region. SAD using $B = \langle 1\,0\,0 \rangle_{Al}$ confirmed that these dendrite arms have the same orientation and therefore belong to the same dendrite. The region containing the eutectic phases is therefore the interdendritic material between these secondary dendrite arms. Similar to the A-DS samples, no crystallographic relationship was found between the aluminum dendrites and any of the eutectic aluminum grains and silicon phases. Also, similar to the A-DS samples, a preferred crystallographic relationship was always observed between each eutectic aluminum grain and the eutectic silicon flake that is partially surrounded by it. Again, similar to the A-DS samples, crystallographic relationships were not found between the eutectic aluminum grain and any of the silicon flakes that lie on its boundaries.

Fig. 12 demonstrates typical results obtained from A-FC samples. Similar to Figs. 10 and 11, the TEM image shown is representative of this alloy and this solidification condition. In this microstructure, there is an alu-

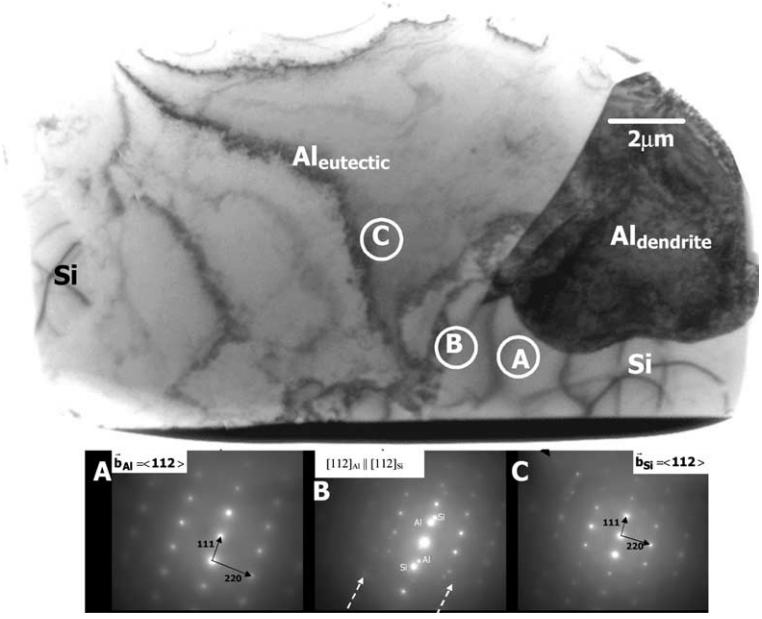

Fig. 12. TEM bright field micrographs of an A-FC casting. $[1\,1\,2]_{Al} \parallel [1\,1\,2]_{Si}$ crystallographic relationship was observed between the eutectic Si and the adjoining eutectic Al. The white circles marked A, B, and C represent the areas where SAD patterns were taken from Si, Si–Al interface region, and Al, respectively. The respective SAD patterns marked A, B, and C are shown in the image. Two white dotted arrows in the SAD pattern taken at the Si–Al interface region show a faint line of Al spots. These spots were clearly visible in the TEM but may not be clear in this image.

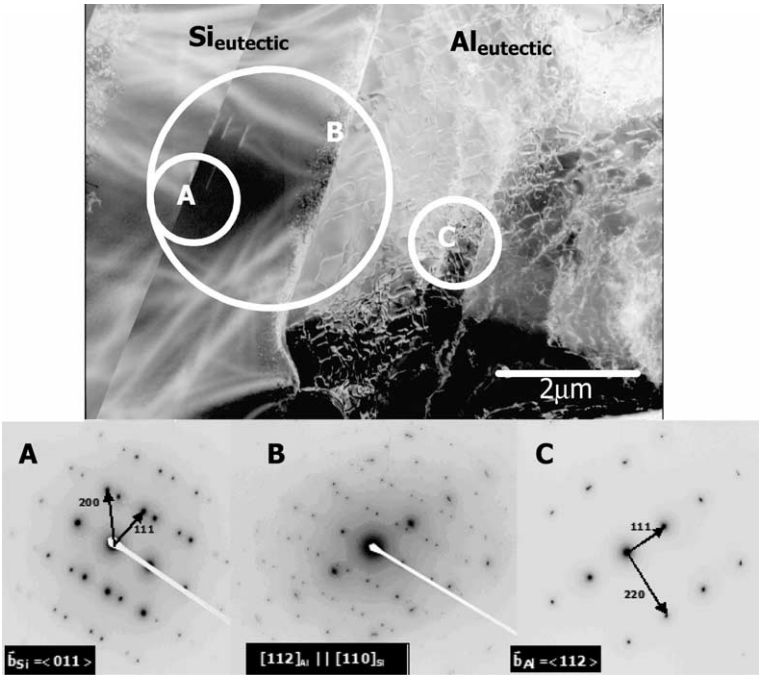

Fig. 13. TEM micrograph of an A-IQ casting. A $[1\,1\,2]_{Al} \parallel [1\,1\,2]_{Si}$ crystallographic relationship was observed between the eutectic Si and the adjoining eutectic Al. The white circles marked A, B, and C represent the areas where diffraction patterns were taken from Si, the Si–Al interface region, and Al, respectively. The respective diffraction patterns marked A, B, and C are shown below the bright field image. It can be seen that the $[1\,1\,2]_{Si}$ and $[1\,1\,0]_{Al}$ overlap well in the pattern taken at the interface region between Al and Si. The images are in inverse polarity mode to enhance viewing contrast.

minum dendrite, one large eutectic silicon flake, a smaller silicon flake, and a large part of a eutectic aluminum grain. Analysis of this and similar samples showed that, similar to the A-DS and A-AC samples, there is no preferred crystallographic relationship between the aluminum dendrites and the eutectic silicon

phase while there is a distinct $[1\,1\,2]_{Al} \parallel [1\,1\,2]_{Si}$ crystallographic relationship between the eutectic aluminum grain and the specific eutectic silicon flake on which it nucleated.

Fig. 13 demonstrates typical results obtained from A-IQ samples. Similar to Figs. 10–12, the TEM image shown is representative of this alloy and this solidification condition. In this microstructure, there is a coarse silicon flake and an adjoining eutectic aluminum grain. Analysis of this and similar samples showed that, similar to the A-DS, A-AC and A-FC samples, there is no preferred crystallographic relationship between the aluminum dendrites and the eutectic silicon phase while there is a distinct crystallographic relationship between the eutectic aluminum grains and the specific eutectic silicon flakes on which each nucleated.

Examination of Figs. 10–13 shows that, while the silicon flakes and the eutectic aluminum grains coarsen as the cooling rate decreases, the crystallographic relationships between the various phases that constitute Al–Si hypoeutectic alloys do not change. There is a crystallographic relationship between eutectic aluminum grains and the specific silicon flakes that nucleate them. This crystallographic relationship (about 70% of the crystallographic relationships found) is the $[1\,1\,2]_{Al} \parallel [1\,1\,0]_{Si}$ relationship. Kobayashi [25] and later Shamsuzzoha [26] observed a similar relationship between eutectic aluminum grains and eutectic silicon flakes in samples where the eutectic growth velocity was about 100 μm/s.

The results of thermodynamic calculations, thermal analyses, and electron microscopy presented in the preceding paragraphs clearly support the proposed theory presented at the beginning of this section and illustrated schematically in Fig. 2.

4. Conclusion

A theory is proposed to describe the nucleation of the eutectic phases in hypoeutectic Al–Si alloys. The proposed theory is based on the fact that Al–Si alloys invariably contain trace amounts of iron, which plays an important role in the nucleation of the eutectic phases. The theory maintains that during the solidification of hypoeutectic Al–Si alloys, primary Al dendrites nucleate at the liquidus temperature, and β-(Al, Si, Fe) particles nucleate in the solute field ahead of the growing aluminum dendrites at a temperature at or above the eutectic temperature of the alloy. Eutectic Si nucleates on these β-(Al, Si, Fe) particles, and eutectic Al nucleates on the eutectic silicon. The growth of the primary aluminum dendrites is arrested when the dendrites impinge on the eutectic Al grains. This mechanism is supported by results of extensive thermal analyses, optical microscopy, scanning and transmission electron microscopy, as well as selected area electron diffraction analyses and elemental X-ray mapping performed on Al–Si hypoeutectic alloy samples of precisely controlled chemistry that were cooled at different cooling rates.

References

[1] Davis JR, editor. Aluminum and aluminum alloys. Ohio: ASM International; 1993. p. 627.
[2] Dash M, Makhlouf M. J Light Met 2002;2:251.
[3] Makhlouf MM, Guthy HV. J Light Met 2001;1:199.
[4] Yilmaz F, Elliott R. J Mater Sci 1989;24:2065.
[5] Dahle AK, Nogita K, Zindel JW, McDonald SD, Hogan LM. Metall Mater Trans A 2001;32:949.
[6] Heiberg G, Nogita K, Dahle AK, Arnberg L. Acta Mater 2002;50:2537.
[7] Crosley PB, Mondolfo LF. Mod Cast 1966;49:89.
[8] Awano Y, Shimizu Y. AFS Trans 1990;176:889.
[9] Jie Wanqi, Chen Zhongwei, Reif W, Mumller K. Metall Mater Trans A 2003;34:799.
[10] Chadwick G. Prog Mater Sci 1963;12:208.
[11] Ho CR, Cantor B. Acta Mater 1995;43:3231.
[12] Zhang DL, Cantor B. Metall Mater Trans A 1993;24:1195.
[13] Ho CR, Cantor B. J Mater Sci Eng A 1993;173:37.
[14] Cantor B. J Mater Sci Eng 1997;151:226.
[15] Murray JL, McAllister AJ. Bull Alloy Phase Diagrams 1984;5:74.
[16] Backerud L, Chai G, Tamminen J. In: Solidification characteristics of aluminum alloys, vol. 2. Olso: AFS/SkanAluminum; 1990.
[17] Shankar S, Riddle YR, Makhlouf MM. Metall Mater Trans A 2003;34:705.
[18] Kurz W, Fisher DJ. In: Fundamentals of Solidification, vol. 27. Switzerland: Trans. Tech. Publications; 1989.
[19] Yang B, Stefanescu D, Leon-Torres J. Metall Mater Trans A 2001;32:3065.
[20] Khalifa W, Samuel FH, Gruzleski JE. Metall Mater Trans A 2003;34:807.
[21] Rivlin GV. Int Met Rev 1981;3:133.
[22] Richards RW. Int Met Rev 1994;39:191.
[23] Mondolfo LF. J Aust Inst Met 1965;10:169.
[24] Bercovici S. In: Proceedings of the 45th international foundry congress, Budapest, Hungary, 1978.
[25] Kobayashi K, Shingu PH, Ozaki R. In: Proceedings of the international conference on solidification and casting of metals, vol. 101. Sheffield, UK, 18–27 July 1977.
[26] Shamsuzzoha M, Hogan LM. J Cryst Growth 1986;76:429.